EUV AND X-RAY OBSERVATIONS OF COMET LOVEJOY (C/2011 W3) IN THE LOWER CORONA

Patrick I. McCauley[1], Steven H. Saar[1], John C. Raymond[1], Yuan-Kuen Ko[2], and Pascal Saint-Hilaire[3]

[1]Harvard-Smithsonian Center for Astrophysics, 60 Garden St, Cambridge, MA 02138
[2]Space Science Division, Naval Research Laboratory, 4555 Overlook Ave., SW, Washington, DC 20375
[3]Space Sciences Laboratory, University of California, Berkeley, CA 94720
Draft version April 8, 2013

ABSTRACT

We present an analysis of EUV and soft X-ray emission detected toward Comet Lovejoy (C/2011 W3) during its post-perihelion traverse of the solar corona on December 16, 2011. Observations were recorded by the Atmospheric Imaging Assembly (AIA) aboard the Solar Dynamics Observatory and the X-Ray Telescope (XRT) aboard Hinode. A single set of contemporaneous images is explored in detail, along with prefatory consideration for time evolution using only the 171 Å data. For each of the eight passbands, we characterize the emission and derive outgassing rates where applicable. As material sublimates from the nucleus and is immersed in coronal plasma, it rapidly ionizes through charge states seldom seen in this environment. The AIA data show four stages of oxygen ionization (O III - O VI) along with C IV, while XRT likely captured emission from O VII, a line typical of the corona. With a nucleus of at least several hundred meters upon approach to a perihelion that brought the comet to within 0.2 $R_\odot$ of the photosphere, Lovejoy was the most significant sungrazer in recent history. Correspondingly high outgassing rates on the order of $10^{32.5}$ oxygen atoms per second are estimated. Assuming that the neutral oxygen comes from water, this translates to a mass-loss rate of $\sim 9.5 \times 10^9$ g s^{-1}, and based only on the 171 Å observations, we find a total mass loss of $\sim 10^{13}$ g over the AIA egress. Additional and supporting analyses include a differential emission measure to characterize the coronal environment, consideration for the opening angle, and a comparison of the emission's leading edge with the expected position of the nucleus.

Subject headings: Comets: general — Comets: individual: C/2011 W3 — Sun: corona

1. INTRODUCTION

Comet Lovejoy (C/2011 W3) is the most significant sungrazer since the launch of the Solar Dynamics Observatory (SDO; Pesnell et al. 2012) and the first to be detected by the X-Ray Telescope (XRT; Golub et al. 2007) aboard Hinode (Kosugi et al. 2007). Its perihelion passage brought the comet to within just 0.2 $R_\odot$ of the photosphere, providing an unprecedented glimpse of a large comet immersed in the lower corona. Lovejoy is a member of the Kreutz family of sungrazing comets, which account for a majority of all sungrazers and are observed in large numbers each year by the Solar and Heliospheric Observatory (SOHO; Domingo et al. 1995). SOHO's Large Angle and Spectrometric Coronagraph (LASCO; Brueckner et al. 1995) has proven a superb discoverer of these objects (Biesecker et al. 2002), having imaged over 1800, and the UltraViolet Coronagraph Spectrometer (UVCS; Kohl et al. 1995) has returned spectra from several Kreutz members (Raymond et al. 1998; Bemporad et al. 2007).

The group is thought to have been formed from the successive fragmentation of a single progenitor as little as 2500 years ago (Sekanina & Chodas 2002, 2004, 2007) and is principally comprised of meter-sized objects that are most often destroyed well before perihelion (Knight et al. 2010). Until Lovejoy, none of the Kreutz members observed by SOHO have survived to emerge from behind the occulting disk of the coronagraph (Iseli et al 2002). A few have made it into the lower corona, but it was not until the launch of SDO in 2010 that they could be followed using the Atmospheric Imaging Assembly (AIA; Lemen et al. 2012). Schrijver et al. (2012) reported the first such observation, which witnessed the destruction of Kreutz fragment C/2011 N3 in July of 2011 about midway through its transit of the solar disk. When Lovejoy followed five months later, it seemed that it would likely meet the same fate, this time behind the Sun from AIA's perspective. Instead, the comet emerged from behind the limb just moments after SDO had finished slewing to its usual disk-center pointing after being off-pointed to observe the ingress.

Exactly how a comet like C/2011 W3 is able to survive its closest approach is still not entirely clear, largely because there is uncertainty regarding its size and composition. Based on the visible magnitude well before perihelion, the nucleus is expected to have been less than ~ 1 km in diameter (Gundlach et al. 2012). Preliminary estimates from SOHO/UVCS suggest a diameter of 400 m upon reaching 6.8 $R_\odot$ during the ingress (Raymond et al. 2013). Finally, after having seemingly escaped, the nucleus was destroyed at ~ 31 $R_\odot$, 1.6 days past perihelion (Sekanina 2012). From mass lost arguments using the visible brightness of the dust tail, Sekanina & Chodas (2012) estimate that the diameter of the nucleus was on order 200 m at the time of its destruction. If the comet's makeup was consistent with the canonical "rubble pile" model, then the tidal forces within the Sun's Roche lobe should have torn it apart opposed only to self gravity and a meager tensile strength. Gundlach et al. (2012) explore
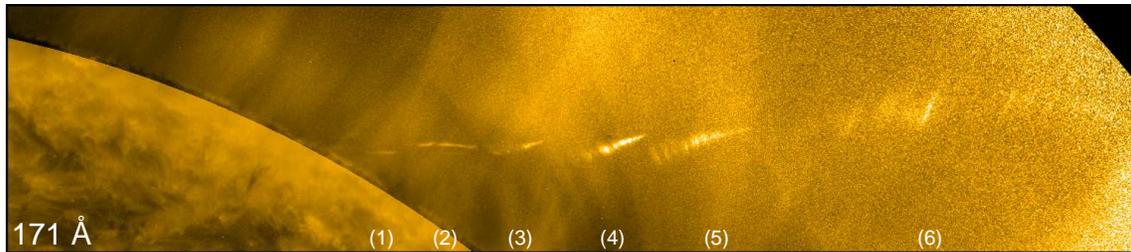
Figure 1. 171 Å AIA images at 6 times: (1) 00:41:36 UT (2) 00:43:00 (3) 00:44:12 (4) 00:46:12 (5) 00:48:12 (6) 00:56:00. We focus this work primarily on multi-wavelength observations at position (4), with some consideration for time evolution in §3.5. These images were produced using a radial filter; see our online material for the corresponding movie.

this possibility and suggest that the cohesive pressure exerted by near-isotropic outgassing could be a sufficient counter to the tidal forces.

However, Sekanina & Chodas (2012) argue that the delayed destruction of the nucleus is evidence that the comet was no "rubble pile" and possessed tensile strength appreciable enough to remain structurally unperturbed by tidal forces. They suggest that the thermal stresses experienced as the comet swept into the lower corona would have taken time to propagate into the interior, after which pockets of water ice would have exploded upon reaching ∼130 K due to an exothermic reaction related to the crystallization of amorphous ice (Schmitt et al. 1989). In this scenario, the comet is destroyed by successive, large fragmentation events rather than steady outgassing. Sekanina & Chodas (2012) include a discussion of preliminary results from the work presented here, which they explain in the context of their fragmentation model. We will revisit this in §4.1.

C/2011 W3 is the first comet to have been detected by a solar X-ray imager, but it is not the first comet to exhibit X-rays at all. Sixteen years ago, Lisse et al. (1996) reported the puzzling detection of extreme ultraviolet (EUV) and X-ray emission from comet C/1996 B2 (Hyakutake) using the X-Ray Telescope aboard ROSAT. Shortly thereafter, such emission was found to emanate from any comet within 3 AU (Dennerl et al. 1997). Cravens (1997) and Krasnopolsky (1997) explained that this high-energy emission arose from charge exchange between solar wind ions and the neutral gas of cometary atmospheres, which are much too cold to produce such energetic photons on their own. But any neutral species are quickly ionized within the AIA and XRT fields of view, so a different mechanism is needed to explain the emission described here.

In their work on the aforementioned C/2011 N3, Schrijver et al. (2012) noted that the EUV emission could be explained by ionization and excitation states experienced as shed cometary material equilibrated with coronal plasma. Bryans & Pesnell (2012) expanded upon this by providing a detailed summary of the means by which sublimated cometary molecules are destroyed and ionized. They constructed a time-dependent model of the cometary emission using a simple geometry and determined which ionization states of which elements would contribute to AIA's EUV channels, noting that these differ significantly from the lines typically important to AIA observations.

We adopt the scenario proposed by Schrijver et al. (2012) and Bryans & Pesnell (2012) and assume that the

EUV and X-ray emission arises from the ionization of cometary material after it is immersed in the corona. Sublimated molecules flow into the coma at velocities of at least a few km s^{-1} (Combi 2000) and are swiftly photodissociated into their atomic constituents. We make the simplifying assumption that water dominates the composition of this material, and since hydrogen does not contribute significantly to any of our passbands, our observations can be largely characterized by which charge states of oxygen contribute most to the various channels. We identify the dominant lines in each of our passbands in §2, which also includes a more thorough discussion of the Bryans & Pesnell (2012) model and how our results compare to theirs.

This paper is structured as follows: §2 describes our observations, the means by which cometary flux was extracted from the coronal background, and the source of EUV and X-ray photons. In §3.1, we use a differential emission measure to probe the coronal environment, and §3.2 details our calculations of outgassing rates from the observed fluxes. The foremost extent of the emission in each channel and the expected position of the nucleus are given in §3.3. §3.4 includes consideration for the 171 Å opening angle, and §3.5 examines time evolution over the egress again using the 171 Å observations. We discuss our work in the context of others in §4. This includes commentary on the Sekanina & Chodas (2012) outburst model, the source of neutral oxygen (water ice vs. dust grains), how our results compare with those of Schrijver et al. (2012) for comet C/2011 N3, and what our results imply about the size of the nucleus. Finally, §5 summarizes our findings.

2. OBSERVATIONS

The observations reported here were taken on December 16, 2011 during the egress of Comet Lovejoy, after it had emerged from behind the solar disk having survived perihelion. Figure 1 provides an overview of our dataset by overlaying six 171 Å AIA images at different times. These images were produced using a radial filter[1], which allows us to see the development of both cometary and coronal emission in one coherent set of images. See our online material for the corresponding movie.

SDO/AIA records images with a 12 s cadence in seven narrowband EUV channels (94, 131, 171, 193, 211, 304,

---

[1] The radial filter divides the off-limb component of an AIA image into concentric rings and scales each ring as a function its radius and brightness relative to neighboring rings. As such, flux is not conserved. The brightness of each pixel corresponds only to its intensity relative to pixels of the same radius. Source code is available in SolarSoft under <aia_rfilter>.
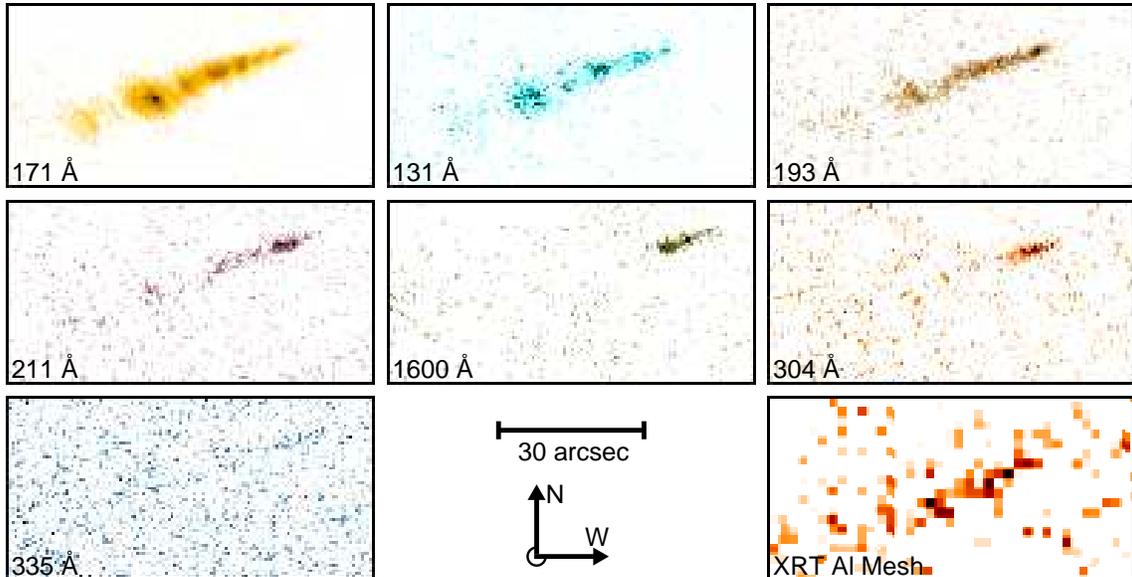
Figure 2. Background subtracted images of the cometary emission at 00:46:12 UT on 2012/12/16. This was ~30 min post-perihelion, corresponding to a height of about 0.56 $R_\odot$ (~320,000 km) above the photosphere. Note that the color tables are inverted, so the darkest regions are those of highest intensity.

& 335 Å) and with a lower cadence in 3 UV bands (1600, 1700, & 4500 Å). The resolution is 0.6″ per pixel over a 4096×4096 px CCD. Detections were made in each channel with the exceptions of the 94, 1700, and 4500 Å bands. Hinode/XRT made successful observations using its thinnest soft X-ray filter, Al-mesh, and recorded non-detections using two thicker filters (Be-med & Al-med). These observations had a cadence of 7 s and a resolution of 2.06″ per pixel. The dominant ions contributing to each channel are listed in Table 1, and discussion of how we arrived at these is given in the next two sections.

Our analysis focuses primarily on a single set of images centered around 00:46:12 UT (position 4 of Fig 1), which is about 30 minutes after perihelion and corresponds to a height above the photosphere of about 0.56 $R_\odot$ (~320,000 km). This height and those quoted later are determined from the most recent ephemeris solution; see §3.3 for additional discussion of the expected trajectory. We chose this time for a strong XRT signal and maximum temporal alignment between XRT and the AIA/171 channel, which was important for characterizing the X-ray production (see §2.3). The thin XRT filters are also affected by CCD contamination spots that attenuate longer X-ray wavelengths, and so this time was also chosen because the location of the comet is free of contamination.

There are a number of interesting features and morphological developments to note as the comet progresses through the AIA field-of-view (FOV) during the egress. These include apparent interactions with the coronal magnetic field (**B**) and spikes in the measured intensity. We will revisit these topics in §3.5, where we consider time evolution using only the 171 Å observations.

2.1. *Background Subtraction*

Background subtraction was necessary to separate cometary and coronal emission. The backgrounds were constructed from averages of 10 frames, 5 before and 5 after the comet appeared within a ~100″ region surround-

ing the emission. Before subtraction, the backgrounds were smoothed using a 5x5 pixel boxcar average to limit the introduction of additional noise. Minor over- and under-subtractions related to intensity gradients across the background frames were accounted for by removing a subsequent linear fit to the column and row averages outside the comet region. Background subtracted images for each channel are displayed in Figure 2.

To extract counts from the comet without including unnecessary background pixels, the flux was taken from a region contoured to the shape of the emission. This was done by thresholding the subtracted images, selecting contiguous pixels, and dilating the resulting mask until it comfortably included all observed emission. Columns 4 and 5 of Table 2 list the results of this. Column 4 includes fluxes integrated over a single, all-encompassing (global) mask, while the values in column 5 were derived from masks individually contoured to the emission in each channel. Note that if the background subtraction were perfect, columns 4 and 5 would be equivalent.

The quoted errors reflect statistical uncertainties based on the total counts recorded for comet and background, along with an additional term that attempts to quantify error from the background removal using the RMS noise outside of the comet region after background subtraction. Columns 6 and 7 list the percentage of the total flux that is attributed to the comet using the global and individual masks, respectively. Note that the difference between these two values is reflective of both the extent of the cometary emission in a given channel and the intensity of the background. Values for the cometary portion of the total flux range between just 3% for the XRT observation and 43% for AIA/131 Å.

2.2. *EUV Emission*

As described in §1, the EUV emission observed by AIA likely arises from the ionization of shed cometary material as it equilibrates with coronal plasma. This material originates from the neutral environment of the nucleus,

Table 1
Dominant Emission Contributors

Ion	Peak[a] log(T) (K)	FWHM[a] log(T) (K)	Ionization[b] Rate q_i (cm^{-3} s^{-1})	Channel[c] (Å)
C IV	5.05	0.35	2.33×10^{-9}	1600
O III	5.1	0.47	1.32×10^{-8}	**304**, 335
O IV	5.3	0.35	5.38×10^{-9}	211, 304
O V	5.4	0.35	1.83×10^{-9}	**171**, 193
O VI	5.55	0.35	6.57×10^{-10}	131, 171, **335**
O VII	6.3	0.47	$\cdots$	Al-Mesh[d]

[a] Temperatures (peak and FWHM range) are based on the G(T) distribution functions from CHIANTI, which represent the temperatures these ions would be associated with under equilibrium conditions. These have been provided for context but are not to be directly associated with the comet observations because the cometary plasma is not in ionization equilibrium.
[b] q_i calculated for log(T) = 6.15 K. Rates for O I and O II are 8.04×10^{-8} and 2.88×10^{-8} cm^{-3} s^{-1}, respectively. See Bryans & Pesnell (2012) for a detailed discussion on ionization rates.
[c] Boldfaced font indicates the more dominant ion for those channels listed twice.
[d] O VII emits near the peak sensitivity of XRT's Al-mesh filter at 22.1 & 21.6 Å. See Fig 4 for the Al-mesh wavelength response.

and thus low ionization states not typically observed by AIA must be considered. We have assumed that the bulk of the sublimated material is water, and since the soon-ionized hydrogen does not contribute significantly to any of the AIA bands, oxygen is the most important atom to consider (see §4.2 for additional discussion on the source of neutral oxygen).

To this end, we have used version 6 of the CHIANTI[2] spectroscopic database (Dere et al. 1997, 2009), coupled with the effective areas of the AIA filters, to determine which O lines dominate each channel. These results are listed in Table 1, and some additional discussion of the emission process is given in §3.2. Note that there are no significant O lines covered by the 1600 Å UV filter, and for this we expect that the emission arises principally from C IV.

Also note that morphological differences between the bands, specifically the length of the tail, result mainly from differences in the ionization times. As we will describe in §3.2, a neutral O atom is stripped of its first electron in about one tenth of a second after being dropped into the coronal plasma. The ionization rate of each subsequent state decreases by a factor of 3–5, and so channels dominated by low charge states (1600 & 304 Å) exhibit shorter tails because these states do not persist for long before ionizing into the next stage. Similarly, the intermediate, O IV image (211 Å) shows an intermediate extent, and likewise for the higher ionization states.

The O VI emission exhibited by the 171 and 131 Å bands will persist until the atoms progress to O VII or the comet-related densities have sufficiently diffused into the coronal background. The next section will show that XRT likely sees material that has indeed made it to O VII, but as will be described in §3.2.1, we suspect that this occurs for only about 1/3 of the O VI atoms. Examination of the O VI images suggests that the cometary

[2] CHIANTI is a collaborative project involving George Mason University, the University of Michigan (USA) and the University of Cambridge (UK).

material becomes indistinguishable from the background after about two minutes near 00:46:12 UT. This time is greatly extended further along in the dataset, likely due to a lower coronal density; see §3.5.1 for additional details.

A more complete assessment of the cometary emission observed by AIA has been carried out by Bryans & Pesnell (2012), who conducted a full, time-dependent analysis with a simple geometry. The coma was modeled as a cylinder populated by concentric shells of successive ionic species, which form as material from the nucleus is sublimated and ionized. Once immersed in the corona, cometary atoms may be ionized in several ways; Bryans & Pesnell include considerations for charge exchange, electron- and proton-impact, and photoionization. Each of these effects is examined for the most abundant elements determined for Comet 1P/Halley by Delsemme (1988), which include H, O, C, N, Si, Fe, Mg, and S (listed here in order of descending abundance). The lines relevant to AIA are identified and displayed in a series of figures showing their emission versus typical quiet-Sun conditions.

Bryans & Pesnell (2012) find that the emission in most channels is dominated by oxygen, and the O ions they identify are consistent with what we present in Table 1 based on our more simplistic approach. The only exception to this is the 335 Å band, for which we find the O VI lines near 131 Å to dominate over the O III lines near 335 Å. We will discuss this further in §3.2.1. Bryans & Pesnell find no significant emission from H, C, N, Si, Mg, or S. They do, however, find that iron contributes significantly to the 171 Å (by ~40%) and 131 Å (~25%) channels. (The 94 Å channel is also found to be dominated by Fe, but a reliable signal was not detected at this wavelength.) The relative contributions of O and Fe in their model depend somewhat on outflow velocity, for which 17 km s^{-1} is used based on observations of C/2011 N3. This dependence is characterized in Figure 10 of their paper and may also be important to our discussion on the source of neutral oxygen in §4.2.

2.3. *Soft X-Ray Emission*

Careful alignment reveals the XRT emission to be offset from AIA. As outgassed material ionizes, its motion soon becomes dominated by the local magnetic field. Newly formed plasma from the comet can be observed drifting along field lines in various directions throughout the AIA dataset (see §3.5.1 for additional details). At 00:46:12 UT, this motion is in a southwest direction that matches the observed offset between nearly simultaneous AIA and XRT images. This is illustrated by Figure 3. The upper panel shows three successive AIA/171 images to establish the direction of motion along the **B** field, while the lower panel shows the XRT offset. The AIA and XRT images in the lower panel have identical start times and are temporally separated only by their respective exposure times of 2.9 and 4.1 s. Given that the motion along the dotted line in Fig 3 is about 0.2″ s^{-1}, the longer XRT exposure cannot explain the offset. We suggest that XRT is seeing material that has flowed down the field lines and further equilibrated with coronal plasma, reaching an ionization state not visible in AIA. The likeliest candidate for this emission is O VII (22.1,
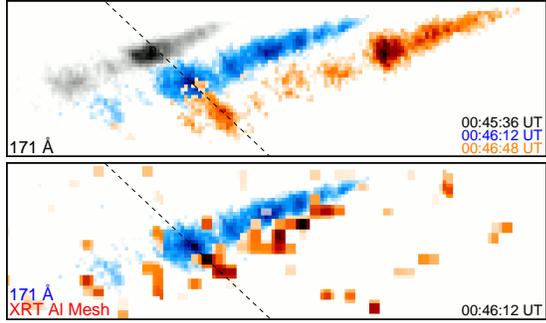
Figure 3. *Top*: 3 successive AIA/171 images, spaced 36 s apart, that demonstrate the direction ionized cometary material travels along the local, coronal **B** field. *Bottom*: Overlay of simultaneous XRT and AIA observations. The XRT emission is offset along the direction established above, suggesting that XRT samples more highly ionized material that has moved farther down the field lines.
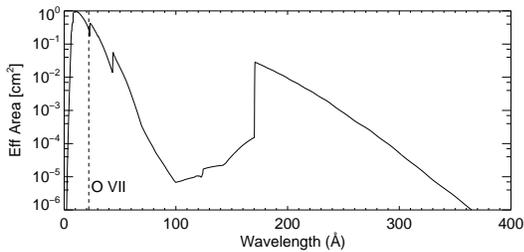

Figure 4. XRT/Al-mesh wavelength response showing the position of O VII lines (dashed line) that likely dominate the cometary emission in this filter.

21.6 Å), which lies near the peak sensitivity of the Al-mesh filter, the wavelength response of which is given in Figure 4. Unlike AIA, XRT is a broadband instrument, and Al-mesh has some sensitivity to each of the lines contributing to AIA's EUV channels. Given the considerable signal exhibited by the 171 Å band in particular, it was initially suspected that the faint XRT signal was also due to EUV emission. But the effective area at these lines is down by a factor of $\gtrsim$100 compared to O VII, and the lower ionization states cannot explain the observed offset. Such an offset would be expected from O VII because of the much longer ionization time compared to O VI (see §3.3 for additional discussion of positional offsets between the emission in each passband).

O VII is a line typical of a moderately active corona. Its temperature distribution function G(T) is peaked around $10^{6.3}$ K with a FWHM of about 1.9 MK. As will be described in §3.1, we find a coronal temperature profile surrounding the comet that is peaked at $10^{6.12}$ K, which would be high enough to generate O VII. It should be noted, however, that G(T) is calculated assuming ionization equilibrium. This assumption cannot be made for the cometary emission, but overlap between G(T) and the coronal temperature profile nonetheless provides some expectation of O VII formation.

3. ANALYSIS

3.1. *Coronal Differential Emission Measure*

To analyze the plasma through which the comet is moving, we have computed a Differential Emission Measure (DEM) for a region surrounding the cometary emission. DEMs summarize coronal temperature and density
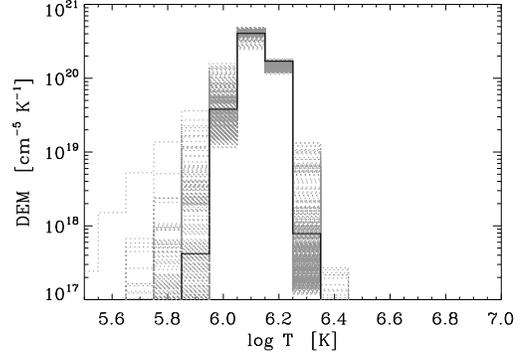

Figure 5. DEM distribution for the corona surrounding the comet at 00:46:12 UT. Solid represents the best fit distribution, while the dotted gray segments indicate Monte Carlo simulations estimating the uncertainty in each log(T) bin.

structure by combining observations of several ions with various characteristic temperatures. This calculation assumes ionization equilibrium and so is not appropriate for the cometary emission itself. Rather, it provides a useful constraint on the conditions that Lovejoy experienced, which is important to our analysis for two reasons: 1) as an input to the outgassing calculations in §3.2, and 2) for discussing the possibility of high-temperature lines like O VII, as in §2.3.

The SolarSoft[3] routine <xrt_dem_iterative2> was used to calculate the DEM using fluxes from the following bands: XRT/Al-mesh and AIA/94, 131, 171, 193, & 211 Å. This software was originally developed for XRT (Weber et al. 2004) and has since be adapted to incorporate AIA data (Cheng et al. 2012).

The approach uses forward-fitting to estimate a DEM that is then fed into the XRT and AIA filter response functions to predict fluxes. The final DEM is found by minimizing the χ^2 between the predicted and observed emission. Monte Carlo simulations are also computed by randomly varying the observed intensities within their RMS noise; the spread of these simulations is then a gauge of the uncertainty (and its distribution) in each log(T) bin. Note that the inclusion of XRT data is particularly important for constraining the high-temperature component, which may be overestimated by DEM solutions that rely solely on AIA.

Input emission counts were taken from a ring immediately surrounding the comet region described in §2. This ring covered an area of 2030 AIA pixels, and the resultant DEM distribution is displayed in Figure 5. We find the coronal environment surrounding the comet at 00:46:12 UT to be characterized by an average temperature of log(T) = 6.15 K, with contributions from plasma between log(T) $\approx$ 5.9 - 6.3 K. The total emission measure covering the full range of temperatures is 1.90×10^{26} cm^{-5}.

3.2. *Outgassing Rates*

As water sublimates from the nucleus, photodissociation of the H_2O molecules produces oxygen atoms that are quickly ionized to charge states typical of the corona. Each O atom lingers in a given charge state for time

Table 2
Measurement Results & Outgassing Rates

Channel (Å)	Photons per Atom at Earth (γN^{-1})	Atoms per Photon at Comet $\log(4\pi \cdot 1AU^2 \cdot N\gamma^{-1})$	Cometary Flux[a] $\log(DN\ s^{-1})$		Cometary Portion of Total Flux		Outgassing Rate[b] $\log(\dot{N})$ [N s^{-1}]	
			Global[c]	Individual[c]	Global[c]	Individual[c]	Global[c]	Individual[c]
1600	1.46	27.28	$2.149 \pm 35\%$	$2.154 \pm 18\%$	6.4%	23%	30.35	30.35
335[d]	0.0032	29.94	$2.002 \pm 47\%$	$1.846 \pm 50\%$	5.5%	7.5%	31.78	31.63
304	0.0021	30.13	$2.399 \pm 22\%$	$2.302 \pm 20\%$	9.9%	16%	32.74	32.64
211	0.0180	29.19	$3.364 \pm 12\%$	$3.290 \pm 11\%$	3.2%	5.1%	32.60	32.52
193	0.0920	28.49	$4.077 \pm 4.9\%$	$4.037 \pm 4.4\%$	4.3%	6.0%	32.57	32.53
171	0.305	27.96	$4.535 \pm 1.4\%$	$4.533 \pm 1.4\%$	21%	21%	32.46	32.46
131[d]	0.0306	28.96	$3.190 \pm 4.4\%$	$3.189 \pm 4.4\%$	43%	43%	31.99	31.99
Al Mesh[e]	$\cdots$	$\cdots$	$2.576 \pm 59\%$		3.1%		$\cdots$	

[a] Fluxes given in measured units. Photons = DN × Gain (e^-DN^{-1}) × 3.65 eV(e^-)$^{-1}$ × $\lambda(hc)^{-1}$, where the CCD gain is ∼18 for the AIA telescopes and 59 for XRT. Taking λ from the dominant lines in Table 1, column 4 converted to $\log(\gamma\ s^{-1})$ is: 3.064, 1.840, 2.609, 3.404, 4.086, 4.495, 3.028, and 2.165. Values are approximate because all contributing λs are not considered. For this reason, we chose to list DN.
[b] $\dot{N}_O$ for all channels except for 1600 Å, which is $\dot{N}_C$.
[c] "Global" results taken from an image mask that encompasses all emission in all channels. "Individual" results taken from masks individually contoured to the emission in each channel.
[d] The 131 and 335 Å results may be underestimates. See §3.2.1 for details.
[e] $\dot{N}_O$ cannot be calculated for O VII because the plasma does not *quickly* ionize through this stage.

$(n_e q_i)^{-1}$, where n_e is the electron density and q_i is the ionization rate for that ion. See Table 1 for q_i and note that a typical coronal n_e of 10^8 cm^{-3} was assumed for the proceeding calculations. Given these values, a neutral O atom is excited to O I in ∼0.12 s.[4] The ionization rate for each subsequent state is 3–5x smaller, and so an ion persists in those states for correspondingly longer durations.

During its time in a given charge state, an atom is excited at rate $n_e q_{ex}$ and produces $q_{ex} q_i^{-1}$ photons, where q_{ex} is the excitation rate. From this and the instrument response to each ion, a total O outgassing rate in atoms per second ($\dot{N}_O$) can be calculated. The calculation is the sum over spectral lines, l, of ions, Z:

$$\text{count rate} = \sum_Z \sum_l A_l \frac{q_{ex,l}}{q_{i,Z}} \dot{N}_O / 4\pi D^2 \qquad (1)$$

Where A_l is the effective area of the AIA band for each line and the distance D is 1 AU.

Outgassing rates are listed alongside their corresponding fluxes in columns 8 and 9 of Table 2. The former shows rates determined via fluxes extracted from a single (global) region that encompasses all emission across all bands, and the latter shows rates determined via fluxes extracted from regions contoured to the shape of the emission in each channel. The second and third columns include important values calculated en route to the final outgassing rates. Column 2 lists the number of photons to be expected at Earth from a given ion before it reaches the next charge state, while 3 lists the number of atoms to be expected at the comet for each photon detected at Earth. For bands containing two ions (see Table 1), the values quoted reflect the sum of both. A pivotal assumption behind these calculations is that the plasma is quickly ionized through each state. Since this is not true of O VII, an outgassing rate cannot be derived from the XRT observations.

---

[4] This time is actually a bit shorter because charge exchange, which we have not accounted for, is a significant ionization mechanism for the lowest stage. Ionization of subsequent states is dominated by electron collisions. See Bryans & Pesnell (2012) for a detailed discussion of this.

Across the EUV channels, we find an average $\dot{N}_O$ of $10^{32.47}$ at 00:46:12 UT (column 9). For comparison, SOHO/UVCS spectra taken at 6.8 $R_\odot$ (∼4.5 hrs before perihelion) suggest $\dot{N}_H = 10^{32.48}$ (Raymond et al. 2013). If all O and H atoms are assumed to come from H_2O, then the UVCS result is down from AIA by about half in $\dot{N}_{H_2O}$. See §4 for additional commentary on these results. A carbon outgassing rate can be similarly estimated from the 1600 Å emission, and for this we find $\dot{N}_C = 10^{30.35}$. This is consistent with expectations based on the Si:O ratio of ∼0.05 observed by UVCS and the C:Si ratio of ∼0.1 reported for fellow Kreutz sungrazer C/2001 C2 (Ciaravella et al. 2010). Note that the rates we derive are somewhat dependent on temperature. For instance, if we were to have assumed $\log(T) = 6.25$ K instead of 6.15 K, the resultant outgassing rates would be about a factor of 1.4 larger.

The $\dot{N}_O$ values derived from the 304, 211, 193, and 171 Å channels agree well, with a standard deviation that is about 18% of their mean for the numbers listed in column 9. However, the rates found from the 335 and 131 Å bands are not so consistent; about a factor of 5 separates the average of these results compared to that of the other EUV channels. Setting this discrepancy, which we will consider in the next section, aside for a moment, the variance in our results could be attributed to a number of factors:

For this analysis, we have assumed that all of the emission arises from the ions listed in Table 1. As noted in §2.2, Bryans & Pesnell (2012) found an appreciable contribution from Fe to the 171 and 131 Å bands that we have not accounted for (∼40 & 25%, respectively). A modest Fe contribution to the 171 Å band would indeed reduce the overall discrepancy somewhat. Likewise, an iron contribution to the 131 Å channel would also bring that result closer the 335 Å value, but whether or not this helps the overall variance depends on the issues discussed in §3.2.1. It is also possible that additional lines unaccounted for in the CHIANTI database are contributing to the observed fluxes, and uncertainties in the calibration of the AIA response to the ions in Table 1 could be

important. However, one of the most significant contributors to the variance in our results is likely atomic rate uncertainties, which are particularly high for EUV lines of the low ionization states being discussed here since it is not often that they must be considered.

3.2.1. *131 and 335 Å Discrepancy*

The oxygen outgassing rates derived from the 131 and 335 Å channels are down by a factor of ∼5 from those found for the other bands. O VI lines at 129–130 Å dominate the predicted count rates for both channels, which are housed together in one of the four AIA telescopes. Each half of the telescope's aperture is coated for a particular channel and is illuminated at all times. Focal-plane filters are used to select the active channel, but the 335 Å filter does not fully reject 131 Å light (Boerner et al. 2012). This is generally a minor effect but is important here because the O III lines near 335 Å are much weaker than their O VI counterparts near 131 Å.

Interestingly, if the 131 Å contribution to the 335 Å response is *not* included, the resultant $\log(\dot{N}_O)$ is found to be 32.49. This is in good agreement with the other bands. If the 131 Å contribution *is* included, then the 335 and 131 Å results agree fairly well with each other, particularly given the 131 Å Fe contribution that has not been included and the low 335 Å signal-to-noise. Regardless of the 335 Å response, the low 131 Å outgassing result must be reconciled with those of the other bands since the atomic rates for O VI should be reliable.

One way to account for this is to assume that, while most of the oxygen atoms progress all the way from O III through O VI, only about 1/3 of them are ionized from O VI to O VII, so that the intensity of the O VI line is only about 1/3 of the value assumed in column 2 of Table 2. This is plausible in that we are looking at a set of images dominated by a short-lived outburst (see §4.1), and the ionization time of O VI is 3× longer than that of O V, which is in turn 4× longer than that of O IV. O VI lines also contribute to the 171 Å band (Bryans & Pesnell 2012), so $\dot{N}_O$ from 171 would have to be increased by perhaps 20%, but this is offset by the Fe IX contribution that we have not included.

If that interpretation is right, $\dot{N}_O$ around $10^{32.5}$ matches all the bands to within a factor of ∼1.5. It implies that less of the oxygen has reached O VII than we had assumed, so a somewhat higher density would be required to account for the XRT count rate. A more complete model of the outgassing rate during the outburst and the time-dependent ionization would improve the estimates, but atomic rate uncertainties of ∼30% and AIA calibration uncertainties limit the ultimate attainable accuracy.

It should also be noted that a higher temperature due to thermalization of kinetic energy from cometary ions would decrease the O VI emissivity relative to that of the other ions somewhat, but not very strongly. However, this would increase the O VII emissivity and the XRT count rate dramatically.
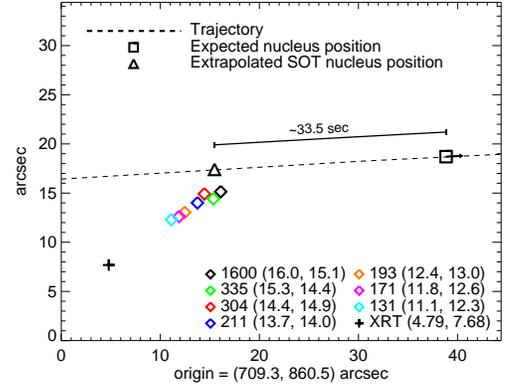

Figure 6. Westernmost, leading edge of the tail in each band surrounding the 171 Å observation at 00:46:12 UT. Trajectory (dotted) and expected nucleus position (square) are taken from JPL orbit solution #58. Extrapolated SOT position (triangle) corresponds to the delay observed by that instrument during the ingress. Parenthetical values in the lower-right indicate positions in arcsec offset from the origin that in turn indicates distance from Sun-center. Note that these positions are shifted based on observation times and the comet's trajectory to estimate locations at 00:46:12 UT.

3.3. *Positional Comparison*

The westernmost, leading tip of the emission in each channel was determined manually, and the results are displayed in Figure 6. Trajectory information is derived from the JPL orbit solution #58 and extracted using the HORIZONS ephemeris generator[5]. Since minor differences in the tip positions can be informative, a few considerations are particularly important. Translational, rotational, and scaling offsets between the four AIA telescopes are accounted for using the <aia_prep> software in SolarSoft. We have used the latest version of this code, which includes refinements to the the telescope offsets resulting from the 2012 Transit of Venus observations. The XRT observations were scaled to AIA's pixel size, rotated to match, and carefully aligned to the limb and on-disk features.

Because the comet is traveling at ∼0.7″s⁻¹ and the observations are spread over 12 s, it is necessary to shift the tip positions found after co-alignment to account for the different observation and exposure times. Shifts were determined using the temporal offsets between the images and the expected motion of the comet according to the JPL ephemeris, which is given as a dotted line in Figure 6. Note that the resolution of AIA is 0.6″px⁻¹ and the alignment between the telescopes is likely good to within 1-2 pixels. Thus, the ∼0.8″ offset between the 131 (light blue) and 171 Å (pink) positions, for instance, is close to the uncertainty from resolution and spatial alignment.

The resultant positions arrange themselves almost exactly as would be expected from emission dominated by the ions listed in Table 1. An exception to this is the 335 Å position. This appears consistent with emission from O III, but as we describe in §3.2.1, we expect this channel to be dominated by O VI. This is a curious but not overly concerning result because, as is evident in Fig 2,

---

[5] http://ssd.jpl.nasa.gov/?horizons

the 335 Å band has very low signal-to-noise, making a precise measurement of the tip position difficult.

C IV (1600 Å) is the first to appear, taking $\sim$1.7 s to reach the fourth ionization stage after being sublimated, given a coronal electron density of 10^8 cm^{-3} and log(T) = 6.15 K. The separation from the nucleus should be $\sim$0.25$\times$ the length of the 1600 Å tail, or about 3.25″. Along a linear fit through tip positions from each pass-band, the distance between the 1600 Å tip and the orbital path is $\sim$3.5″. We therefore see about a 28 s delay between the expected nucleus position and that suggested by the AIA observations.

The Solar Optical Telescope (SOT) aboard Hinode also observed the comet during its ingress on the opposite side of the solar disk. The observed position was precisely along the expected orbital path but $\sim$33.5 s behind the predicted position. The extrapolated SOT position based on this delay is denoted by a triangle in Figure 6, and one can see much better agreement between this position and the expectation from AIA. Ground-based observations well outside perihelion were used to construct the ephemeris, so the solution very near the Sun may suffer a small timing error as a result. It should be also be noted that the orbit determination for Comet Lovejoy is still ongoing, so agreement between the ephemeris and the solar telescope observations will likely improve.

The distance (d) between the tips seen in O III and VI (304 and 131 Å) can also be used to estimate the density of the emitting plasma:

$$d \approx V_{\text{comet}} * n_e^{-1}(q_{\text{III}}^{-1} + q_{\text{IV}}^{-1} + q_{\text{V}}^{-1}) \qquad (2)$$

Where the ionization rate coefficients q_i are those given in Table 1. Following from this, we find an electron density of $\sim$1.4$\times10^8$ cm^{-3}.

3.4. *Opening Angle*

The opening angle of the tail is informative of the interplay between outgassed material and the local magnetic field. It can be well-measured in the 171 Å images, which exhibit the highest signal-to-noise. To do this, we manually determine a vector that roughly bisects the emission and is perpendicular to the striations along which cometary material is collected by the magnetic field (further discussion of these striations can be found in §3.5.1). The emission is then divided into slices perpendicular to this vector, a Gaussian is fit to the emission along each slice, and the width of the comet at each location is determined by the distance between the 3-σ levels on either side of the Gaussian distribution. From this, we find the opening angle of the 171 Å emission at 00:46:12 UT to be 12.8°.

For Lyman-alpha images of sungrazing comets at larger heights, the interpretation of the opening angle is straightforward (Bemporad et al. 2005): Hydrogen atoms from the dissociation of cometary water exchange electrons with coronal protons, producing a cloud of neutrals that have the temperature and velocity of the local coronal environment. The cloud expands at the thermal speed, producing a cone with opening angle $\tan^{-1}(V_{\text{thermal}}/V_{\text{comet}})$.

The case of Comet Lovejoy is more complex. An oxygen atom is moving at V_{comet} upon release from the nucleus. As it becomes ionized and begins to interact with the coronal magnetic field, the O atom behaves like a pickup ion in the solar wind (Gloeckler & Geiss 2001). The velocity component perpendicular to the field becomes a gyration speed, $V_{\perp}$, and the parallel component is conserved as $V_{\parallel}$. Since all the ions have nearly the same speed, they form a tight ring in velocity space. This ring distribution is very unstable and quickly scatters into a bispherical shell distribution with components of two intersecting shells centered at $V_{\parallel} \pm V_A$, where V_A is the Alfvén speed (Williams & Zank 1994).

Thus, after deprojection from plane-of-the-sky to true values, the angle between the comet's path and the center of its tail gives $V_{\parallel}$ / V_{comet}. And the opening angle of the tail gives the width of the bispherical distribution, which depends on V_A, V_{comet}, and the angle between V_{comet} and **B**. That analysis is beyond the scope of this paper because it requires knowledge of the **B** field direction and because the bispherical shell may further scatter, exchanging energy and momentum with the coronal plasma.

3.5. *Time Evolution*

This section is intended as a prelude to future work that will cover the time evolution of Comet Lovejoy in more detail. Here we make some qualitative remarks about morphological developments during the egress, followed by a quantitative analysis of the AIA/171 flux versus time.

3.5.1. *Morphological Developments*

A number of interesting features in this dataset bear mentioning. We do so here with references to the positions labeled in Figure 1, but readers would be best served by downloading the corresponding movie available in our online material. Traveling roughly horizontally with respect to the FOV, the comet emerged from behind the limb $\sim$25 min after perihelion. Interaction between shed cometary material and the local magnetic field is immediately apparent, as a parcel of newly-formed plasma can be seen traveling away from the Sun along a radial field system near position 1. Ionized cometary material will tend to spiral along field lines with a speed that depends on V_{comet} and the angle between V_{comet} and **B**. For this initial interaction, the component of V_{comet} along **B** appears to be greatest, so we observe the swiftest motion of cometary material along field lines here. Similar, but slower, motions can be observed near positions 4 and 5 in a southwestern direction and in a northwestern direction near position 6.

In position 2, we see the tail stretched out in a slight, inverted u-shape. This appears to be the comet skimming overtop of underlying loops, but modeling of the magnetic field will be needed to understand this. The same is true for the vertical striations that become most pronounced after position 4, which can be interpreted as newly formed plasma being arranged along field lines. As was pointed out by Bryans & Pesnell (2012), such striations are also visible during the ingress. Other groups are working on magnetohydrodynamic (MHD) modeling of this system, and it will be interesting to see how closely correlated these striations are with the model field predictions.

Position 6 shows the last frame for which the leading edge of the EUV emission can be traced before it has
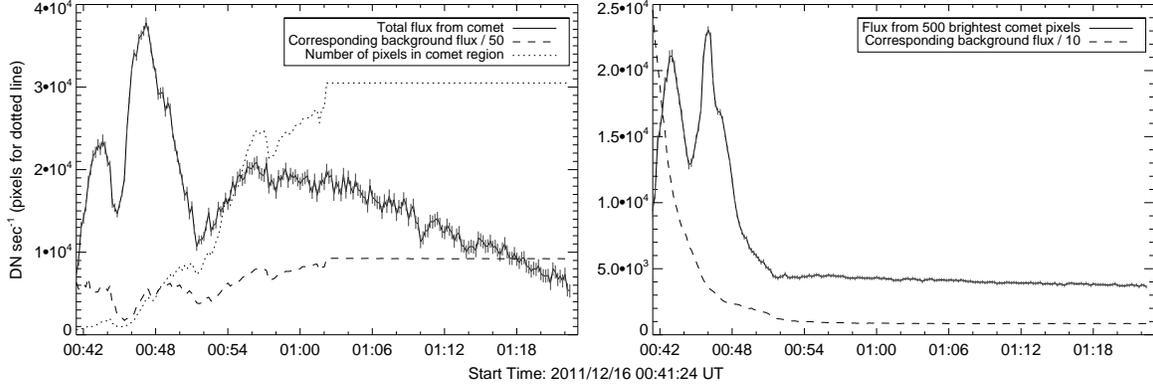
Figure 7. *Left*: Total 171 Å cometary flux (solid) alongside corresponding background emission divided by 50 (dashed) and area of emission region in pixels (dotted). *Right*: Total 171 Å flux from the 500 brightest comet pixels (solid) alongside flux from corresponding background pixels divided by 10 (dashed). Perihelion occurred ∼25 min prior to the plots' start time, and the leading edge of the tail exits the FOV at 00:56:00 UT. 00:41:00 and 00:56:00 UT correspond to heights above the photosphere of 0.46 and 0.78 R$_\odot$, respectively.

left the FOV. This occurs at about 00:56:00 UT when the comet is ∼0.56 R$_\odot$ above the photosphere. Emission visible in the radial filter movie lingers along the striations at this position for another ∼40 minutes. The motion of these striations during this period is very interesting, with the roughly vertical threads pulling apart and moving together in a manner reminiscent of aurorae on Earth.

3.5.2. *Flux vs. Time*

Figure 7 quantifies the 171 Å brightness over a 40-minute period from 00:41:24 through 01:22:24 UT. This begins about 25 minutes after perihelion, corresponding to a height of ∼0.46 R$_\odot$ above the photosphere, and ends ∼26 minutes after the leading edge of the tail has left the FOV. The solid line in the left panel shows the total flux extracted after background subtraction from a region contoured to fit the cometary emission. The dashed line indicates the total background flux from the same region, and the dotted line shows the area of this region in pixels.

The background subtraction and region selection for this analysis was done in the same manner as described in §2 with some modifications. Since the tail's extent and position changes from frame-to-frame, a new "comet region" (mask) must be selected for each image. To make the evolution of this region as continuous as possible, the mask for each frame was taken from the previous image and adjusted to fit the new extent. The dotted line in the left panel of Fig 7 indicates the area of this mask, showing the dramatic rise of the emission's extent as time progresses. Note that the background flux in the left panel (dashed line) is largely dependent on the area indicated by the dotted line. Though coronal emission falls off exponentially with radial distance, the size of the comet mask increases nearly as fast, yielding a relatively constant background flux when integrated over the entire region.

To display these data in a manner independent of the mask size, the right panel of Fig 7 shows the cometary flux integrated over only the 500 brightest pixels in the the selected region (solid line). The dashed line again shows the background flux integrated over the same pixels used for the solid line. Since a constant area is being used, the background curve drops off as would be expected of the corona.

As previously noted, the leading edge of the tail can

be seen exiting the FOV at about 00:56:00 UT, which corresponds to a local maximum in the comet's flux as shown in the left panel of Fig 7. After this time, lingering emission drifts about for many minutes confined to a region somewhat larger than the extent indicated by position 6 in Fig 1. The frame-by-frame evolution of the comet mask is discontinued after 01:02:00 UT in favor of a constant region; the flat portion of the dotted line in the left panel of Fig 7 results from this.

We find the AIA/171 brightness to be characterized by three distinct peaks and leave their interpretation to the proceeding section, where we discuss the profiles shown in Fig 7 in the context of the outburst model proposed by Sekanina & Chodas (2012). The total integrated emission under the flux vs. time plot in Fig 7 is log(I) = 7.609 DN, which implies to a total outgassing of $10^{35.53}$ oxygen atoms based on the 171 Å production rates listed in Table 2. Note that in applying the Table 2 rates to the integrated flux, we are in effect assuming that the corona is of uniform temperature and density throughout the AIA FOV. If entirely from water, our total outgassing result translates to a mass loss of ∼1.0×10^{13} g. For comparison, Sekanina & Chodas (2012) used dust observations to estimate a residual mass of the nucleus of ∼1×10^{12} g after its destruction 1.6 days post-perihelion at 31 R$_\odot$. We will discuss the implications of our mass loss estimate on the expected size of the nucleus in §4.4.

4. DISCUSSION

4.1. *Outbursts*

Sekanina & Chodas (2012) used preliminary results from this study, presented at the 2012 Summer AAS meeting, to test their model for the process by which Comet Lovejoy's nucleus may have been destroyed, which was touched on in §1. In summary, they contend that the nuclei of sungrazers like this one are principally destroyed through successive, large fragmentation events, rather than by steady outgassing. As heat propagates into the interior of the nucleus, pockets of water ice explode, calving off large chunks of material in outburst events. This results from an exothermic reaction triggered by the crystallization of amorphous ice at a critical temperature of ∼130 K (Schmitt et al. 1989). Such an interpretation is significant to our general understanding of cometary compositions because it implies that the nu-

cleus has a tensile strength far greater than what would be implied by the canonical "rubble pile" model.

In our AAS poster, we performed the outgassing calculations described in §3.2 at three times (2012/11/16 00:44:12, 00:46:12, and 00:48:12 UT), and these results began to trace out the second of the two sharp peaks in Fig 7. Sekanina & Chodas note that these rates could not be sustained by a sub-kilometer nucleus for very long. Instead they suggest that without drastically increasing the expected size of the nucleus, our results could only be explained in the context of an outburst, perhaps one of the four post-perihelion events that they suspect ultimately led to the total destruction of the nucleus.

With the fuller analysis presented in §3.5.2, we see that the 171 Å intensity is characterized by three distinct peaks, the first two of which are sharp spikes that occur while the emission is confined to a relatively compact region spanning less than ∼50″. These are centered near 00:43:00 and 00:47:00 UT, respectively, and we find them to be consistent with the outburst model proposed by Sekanina & Chodas (2012). It is apparent from the two-peaked profile that material was expelled from the nucleus in distinct phases, but whether or not this implies explosions in distinct pockets of water ice is unclear. Further evidence for the outburst scenario may be found in the relative contributions of O and Fe to the observed emission. This would be informative of the source of neutral oxygen, which may be either water ice (as we have assumed) or dust grains (as proposed by Sekanina & Chodas). We discuss these possibilities in the next section.

Though the overall intensity of the third peak at 00:56:00 UT is comparable to the first two, the emission is far more diffuse and the rise more gradual than the earlier peaks, which are dominated by dense collections of very bright pixels. If the first two spikes are the result of outbursts that ejected large volumes of material from the nucleus, then we speculate that third peak may arise from more gradual outgassing through newly opened vents. Since the front of the tail leaves the FOV at the time of the third peak, we may also be seeing the beginning of a much longer rise phase. Even if this were true, the nature of this event does not appear to be quite the same as the first two because dense concentrations of material are not observed.

There is also a question of why the emission lingers for so long near the FOV edge when this behavior is not found to the same extent earlier. We suspect this to be primarily a result of density contrast. The coronal density is likely much less at this location than closer in, so the time it takes for the cometary material to diffuse into the background is much longer. This is coupled with the fact that a lower density and likely temperature will increase ionization times, so we see material progressing into and leaving the charge states observable at 171 Å more slowly.

4.2. Oxygen Source

Sekanina & Chodas (2012) have suggested that much of the oxygen seen in the AIA images originates from the vaporization of cometary dust grains rather than sublimation of water ice. From an observational standpoint, the two possibilities can be distinguished if the very high abundances of Si, Mg, and Fe relative to O in dust imply significant emission in some of the AIA channels. We take the Mg:Si and Fe:Si abundance ratios to be 0.69, as did Bryans & Pesnell (2012) based on the abundances in Comet Halley (Delsemme 1988). Assuming that the Si:O ratio is 0.5, we used Version 7 of CHIANTI (Dere et al. 1997; Landi et al. 2012) to compute contributions of the refractory elements. This ratio is what we would expect if the dominant oxygen source is dust grains; note that it is an order of magnitude higher than what we reference in §3.2.

Si would produce only 10% increases in the AIA bands except for the 94 Å band, where it would provide a large fractional increase but still leave the emission at an undetectable level. Mg would increase the brightness in the 304 and 335 Å bands by about a factor of 3, which would aggravate the disagreement among the channels. It would also make the 304 Å image appear longer and more displaced from the comet nucleus than observed.

If we assume that $n_e t$ is large enough to ionize O through O VI, it will also ionize Fe through Fe IX. In that case, Fe VIII and Fe IX make substantial contributions to a few bands, particularly at 171 Å. A modest contribution reduces the discrepancy among the channels, but if the oxygen comes from dust grains, the expected iron levels would increase the 171 Å brightness by a factor of six, pushing it out of line with the other channels. An Fe:O ratio of about 0.05 seems to give the best agreement, suggesting a grain-to-water ratio of about 1/6. This is in line with the Si:H ratio obtained from the UVCS spectrum at 2 $R_\odot$ during the ingress (Raymond et al. 2013).

It is important to note that this discussion pertains to the frames we have analyzed in detail. These were centered around 00:46:12 UT, which lies near the peak intensity indicated by Fig 7. We have suggested that this peak is consistent with the outburst scenario proposed by Sekanina & Chodas (2012). If true, then the intensity spike results from the explosion of an interior pocket of water ice that blew off a chunk of the nucleus. Sekanina & Chodas point to dust grains as the primary source of neutral oxygen because they suspect most surface ice to have already been sublimated away by the time of these observations, with the only significant source of H_2O left being these interior reservoirs.

If this type of outburst is manifested in the AIA data, then presumably the ejecta contains high concentrations of water, which would be consistent with our results. It may also be true that when not in an outburst phase, the primary source of neutral oxygen is indeed dust grains. As we have just described, this could be determined by the relative contribution of Fe implied by outgassing rates derived near a minimum in the overall intensity versus that found for the maximum period this paper has focused on. If dust was found to be the dominant source of neutral O outside of the peak phase, this would also strengthen the notion that the intensity spike results from an explosion of interior water ice. These questions will be addressed in a followup study that will cover time evolution in more detail.

4.3. Comparison with C/2011 N3

As has been previously mentioned, the first sungrazing comet observed by AIA came a few months prior to

Lovejoy when fellow Kreutz member C/2011 N3 burned up midway through its transit of the solar disk. These results were published by Schrijver et al. (2012), which was discussed briefly in §1. As with Lovejoy, emission from C/2011 N3 was detected in all of AIA's EUV channels except at 94 Å.

Schrijver et al. also estimated the mass loss of C/2011 N3 but did so in a very different manner than through the outgassing calculations presented here. They measured the deceleration of material lost from the nucleus and coupled this with the comet's orbital trajectory and approximate knowledge of the coronal plasma density to estimate a mass loss rate of $(0.01\text{-}1)\times10^8$ g s^{-1} over the duration of the comet's visibility to AIA. This amounted to a total mass loss of $\sim6\times10^8$ to 6×10^{10} g.

In §3.2, we estimate an average $\dot{N}_O$ of $10^{32.5}$ across the AIA channels for the C/2011 W3 at 00:46:12 UT. Assuming all this comes from water, we have a mass loss rate of $\sim9.5\times10^9$ g s^{-1} (see §4.2 for discussion on the source of neutral O). Note that this time lies near the peak intensity indicated by Fig 7. Aside from the first few frames, for which some of the emission may be hidden behind the solar disk, the minimum intensity observed before the leading edge of the 171 Å emission exited the FOV occurred at 00:52:24 UT and was down by a factor of ~3.2x from 46:12. For this time, we estimate $\dot{N}_O$ to be $10^{31.95}$, which translates to a mass lost rate of 2.7×10^9 g s^{-1}. As noted in §3.5.2, our total mass loss is estimated at $\sim10^{13}$ g.

Our results are obviously considerably higher than what was reported for C/2011 N3, which was to be expected given that Lovejoy was a considerably larger comet. Schrijver et al. estimated that the nucleus of C/2011 N3 was between 10 and 50 meters during the AIA visibility, while Lovejoy was estimated at somewhat less than 1 km upon its solar approach (Gundlach et al. 2012). Initial estimates from SOHO/UVCS spectra point to a diameter of 400 m by the time the comet reached 6.8 $R_\odot$ pre-perihelion (Raymond et al. 2013). So at the time of our observations, Lovejoy's nucleus was likely at least an order of magnitude larger in diameter than C/2011 N3. Given this, a peak mass loss rate that is a bit more than an order of magnitude larger than what was derived for C/2011 N3 from a very different method is an encouraging result. We discuss the size of the nucleus implied by our own results in the next section.

4.4. Size of the Nucleus

The size of the nucleus at the start of our dataset can be inferred from the total mass loss of $\sim10^{13}$ g that we estimate in §3.5.2. To do this, we must first make an assumption about bulk density. Like Sekanina & Chodas (2012), we take the bulk density to be 0.4 g cm^{-3} based on the Deep Impact results from Comet 9P/Tempel 1 (Richardson et al. 2007). This result ranged from 0.2–1 g cm^{-3} with a preferred value of 0.4, and how well it applies to Comet Lovejoy is uncertain. See the review by Weissman & Lowry (2008) for a conglomeration of various cometary density estimates, which suggested a "best" average value of 0.6 g cm^{-3}. At 0.4 g cm^{-3}, our mass loss translates to a sphere of diameter ~363 m.

Sekanina & Chodas (2012) estimate that the nucleus was between 150 and 200 m in diameter at the time of its destruction 1.6 days after perihelion. Allowing for some outgassing after the comet left the AIA field-of-view, we find that the nucleus was at least 400 m in diameter when our observations begin, 25 minutes post-perihelion. Our mass loss estimate then corresponds to the erosion of a ~73 m layer from the surface, leaving the nucleus with a diameter of ~254 m when it exits the AIA FOV. At this size, another $\sim(1.7\text{–}2.7)\times10^{12}$ g of material could be lost before reaching the 150–200 m diameter found by Sekanina & Chodas.

Considering the unknown amount of mass lost behind the Sun and on ingress, the nucleus may then have been around 600 m in diameter before the encounter. This would allow for just over 3 times the total outgassing derived here (3×10^{13} g) to be sustained before the start of our observations. Note that this estimate is somewhat larger than the 400 m preliminary estimate from SOHO/UVCS at 6.8 $R_\odot$ pre-perihelion (Raymond et al. 2013).

5. CONCLUSION

We have explored the EUV and X-ray emission observed toward Comet Lovejoy using post-perihelion observations from AIA and XRT. Our results are summarized by the following bullet points:

- We find the emission to be dominated by oxygen ions with some contribution from iron, as proposed by Bryans & Pesnell (2012). These ions form as neutrals from the comet sublimate, dissociate, and ionize toward equilibrium with coronal plasma. We also note that, unlike the other channels, carbon dominates the 1600 Å band. [§2]

- O III through VI are observed in the AIA EUV bands, along with C IV in the 1600 Å UV channel. These findings are based on cometary abundances, the lines listed in CHIANTI, and the effective areas of the AIA filters. [§2.2]

- O VII is observed by XRT. This conclusion is based on the spatial offset between the tail observed in XRT and AIA, the wavelength response of the Al-mesh filter, and expectations based on the coronal environment. [§2.3]

- A DEM analysis of the background corona finds Lovejoy's environment at 00:46:12 UT to be characterized by an average $\log(T) = 6.15$ K, with a total emission measure of 1.90×10^{26} cm^{-5}. [§3.1]

- We find an average outgassing rate ($\dot{N}_O$) of $10^{32.47}$ across the EUV channels at 00:46:12 UT. This calculation is a function of the coronal temperature and electron density, the ionization and excitation rates for each species, and the instrument response to each ion. [§3.2]

- From the 1600 Å channel, we find $\dot{N}_C = 10^{30.35}$. This is consistent with expectations based on the Si:O and C:Si ratios found by UVCS for another Kreutz sungrazer. [§3.2]

- A positional comparison of the leading edge of the tail in each channel further suggests the emission

is dominated by the species we identify. It also suggests that the location of the nucleus is ∼28 s delayed from expectations based on JPL orbit solution #58. [§3.3]

- $n_e \approx 1.4 \times 10^8$ cm^{-3} is found for the cometary plasma based on the distance between the O III and VI (304 and 131 Å) tips. [§3.3]

- An opening angle of 12.8° is found for the 171 Å tail at 00:46:12 UT. We note that this angle differs from that of Ly-α tails because O ions at low heights will behave like pickup ions in the solar wind, forming a complex distribution that depends on V_{comet}, V_A, and $\mathbf{B}$. [§3.4]

- We quantify the AIA/171 brightness and find it to be characterized by 3 distinct peaks in intensity, with a factor of ∼3.5 separating the high and low values observed while the leading edge of the tail remained in AIA's FOV. [§3.5]

- Integrating under the AIA/171 flux vs. time plot, we find log(I) = 7.609 DN. This translates to $10^{35.53}$ oxygen atoms and a mass loss of ∼10^{13} g, assuming that the oxygen comes from water and the background corona is of uniform temperature and density. [§3.5]

- We find the AIA/171 flux vs. time results to be consistent with the outburst interpretation of our preliminary results by Sekanina & Chodas (2012). [§4.1]

- We dispute the notion presented by Sekanina & Chodas (2012) that the O ions observed around 00:46:12 UT arise principally from vaporized dust grains rather than sublimated water. We base this on the relative outgassing rates found, noting that the 171 Å brightness should be much greater if the O atoms come from dust because of the much higher Fe contribution implied. [§4.2]

- Comparing our results to those of Schrijver et al. (2012) for C/2011 N3, we find a peak mass loss rate that is over an order of magnitude greater for Comet Lovejoy (9.5×10^9 vs. 1×10^8 g s^{-1}), which is consistent with expectations based on Lovejoy's much larger size. [§4.3]

- Based on our total mass loss estimate of 10^{13} g, we suggest that the nucleus was at least 400 m in diameter at the start of our observations, 25 min after perihelion. At a bulk density of 0.4 g cm^{-3}, this is equivalent to the erosion of a 73 m surface layer, leaving the nucleus at ∼254 m upon exiting the AIA FOV. [§4.4]

The AIA and XRT observations of Comet Lovejoy have provided an exciting new entry into the study of sungrazing comets. Several groups continue to work on this dataset, and a followup to this study will be prepared in the coming year. AIA and XRT are also poised to obtain similar images for the upcoming perihelion passage of Comet 2012 S1 (ISON), which appears to be 5 to 10 times larger than Lovejoy and will reach its closet approach on November 28th, 2013.

REFERENCES

Bemporad, A., Poletto, G., Raymond, J. C., Biesecker, D. A., Marsden, B., Lamy, P., Ko, Y.-K., & Uzzo, M. 2005, ApJ, 620, 523

Bemporad, A., Poletto, G., Raymond, J., & Giordano, S. 2007, Planet. Space Sci., 55, 1021

Biesecker, D. A., Lamy, P., St. Cyr, O. C., Llebaria, A., & Howard, R. A. 2002, Icarus, 157, 323

Boerner, P., Edwards, C., Lemen, J., et al. 2012, Sol. Phys., 275, 41

Brueckner, G. E., Howard, R. A., Koomen, M. J., et al. 1995, Sol. Phys., 162, 357

Bryans, P. & Pesnell, W. D. 2012, ApJ, 760, 18

Cheng, X., Zhang, J., Saar, S. H., & Ding, M. D. 2012, ApJ, 761, 62

Ciaravella, A., Raymond, J. C., & Giordano, S. 2010, ApJ, 713, L69

Combi, M. 2000, Earth, Moon & Planets, 89, 73

Cravens, T. E. 1997, Geophys. Res. Lett., 24, 105

Delsemme, A. H. 1988, Royal Society of London Philosophical Transactions Series A, 325, 509

Dennerl, K., Englhauser, J., & Trümper, J. 1997, Science, 277, 1625

Dere, K. P., Landi, E., Mason, H. E., Monsignori Fossi, B. C., & Young, P. R. 1997, A&AS, 125, 149

Dere, K. P., Landi, E., Young, P. R., Del Zanna, G., Landini, M., & Mason, H. E. 2009, A&A, 498, 915

Domingo, V., Fleck, B., & Poland, A. I. 1995, Sol. Phys., 162, 1

Gloeckler, G. & Geiss, J. 2001, Space Sci. Rev., 97, 169

Golub, L., DeLuca, E., Austin, G., et al. 2007, Sol. Phys., 243, 63

Gundlach, B., Blum, J., Skorov, Yu. V., & Keller, H. U. 2012, arXiv:1203.1808v1 [astro-ph.EP]

Iseli, M., Küppers, M., Benz, W., & Bochsler, P. 2002, Icarus, 155, 350

Knight, M. M., A'Hearn, M. F., Biesecker, D. A., Guillaume, F., Hamilton, D. P., Lamy, P., & Llebaria, A. 2010, A&A, 139, 926

Kohl, J. L., Esser, R., Gardner, L. D., et al. 1995, Sol. Phys., 162, 313

Kosugi, T., Matsuzaki, K., Sakao, T., et al. 2007, Sol. Phys., 243, 3

Krasnopolsky, V. 1997, Icarus, 128, 368

Landi, E., Del Zanna, G., Young, P. R., Dere, K. P., & Mason, H. E. 2012, ApJ, 744, 99

Lemen, J. R., Title, A. M., Akin, D. J., et al. 2012, Sol. Phys., 275, 17

Lisse, C. M., Dennerl, K., Englhauser, J., Harden, M., Marshall, F. E., Mumma, M. J., Petre, R., Pye, J. P., Ricketts, M. J., Schmitt, J., Trumper, J., & West, R. G. 1996, Science, 274, 205

Pesnell, W. D., Thompson, B. J., & Chamberlin, P. C. 2012, Sol. Phys., 275, 3

Raymond, J. C., Fineschi, S., Smith, P. L., Gardner, L., O'Neal, R., Ciaravella, A., Kohl, J. L., Marsden, B., Williams, G. V., Benna, C., Giordano, S., Noci, G., & Jewitt, D. 1998, ApJ, 508, 410

Raymond, J. C., et al. 2013, in preparation.

Richardson, J. E., Melosh, H. J., Lisse, C. M., & Carcich, B. 2007, Icarus, 190, 357

Schmitt, B., Espinasse, S., Grim, R. J. A., Greenberg, J. M., & Klinger, J. 1989, in Physics and Mechanics of Cometary Materials, ed. J. Hunt & T. D. Guyenne (ESA SP-302; Noordwijk, The Netherlands: ESTEC), 65

Sekanina, Z. 2012, CBET, 2967, 1

Sekanina, Z. & Chodas, P. W. 2002, ApJ, 581, 1389

Sekanina, Z. & Chodas, P. W. 2004, ApJ, 607, 620

Sekanina, Z. & Chodas, P. W. 2004, ApJ, 663, 657

Sekanina, Z. & Chodas, P. W. 2012, ApJ, 757, 127

Schrijver, C. J., Brown, J. C., Battams, K., Saint-Hilaire, P., Liu, W., Hudson, H., & Pesnell, W. D. 2012, Science, 335, 324

Weber, M. A., DeLuca, E. E., Golub, L., & Sette, A. L. 2004, in IAU Symposium, Vol. 223, Multi-Wavelength Investigations of Solar Activity, ed. A. V. Stepanov, E. E. Benevolenskaya, & A. G. Kosovichev, 321-328

Weissman, P. R., & Lowry, S. C., 2008, Meteor. Planet. Sci., 43, 1033

Williams, L. L. & Zank, G. P. 1994, J. Geophys. Res., 99, 19229